

Sequential Molecular and Cellular Events during Neoplastic Progression: A Mouse Syngeneic Ovarian Cancer Model¹

Paul C. Roberts*, Emilio P. Mottillo*,[†] Andrea C. Baxa*, Henry H. Q. Heng[‡], Nicole Doyon-Reale*, Lucie Gregoire*,[†] Wayne D. Lancaster^{†,‡}, Raja Rabah[§] and Eva M. Schmelz[†]

*Department of Immunology/Microbiology, School of Medicine, Wayne State University, Detroit, MI 48201, USA;

[†]Karmanos Cancer Institute, School of Medicine, Wayne State University, Detroit, MI 48201, USA; [‡]Center for Molecular Medicine and Genetics, School of Medicine, Wayne State University, Detroit, MI 48201, USA;

[§]Department of Pathology, School of Medicine, Wayne State University, Detroit, MI 48201, USA

Abstract

Studies performed to identify early events of ovarian cancer and to establish molecular markers to support early detection and development of chemopreventive regimens have been hindered by a lack of adequate cell models. Taking advantage of the spontaneous transformation of mouse ovarian surface epithelial (MOSE) cells in culture, we isolated and characterized distinct transitional stages of ovarian cancer as the cells progressed from a premalignant nontumorigenic phenotype to a highly aggressive malignant phenotype. Transitional stages were concurrent with progressive increases in proliferation, anchorage-independent growth capacity, *in vivo* tumor formation, and aneuploidy. During neoplastic progression, our ovarian cancer model underwent distinct remodeling of the actin cytoskeleton and focal adhesion complexes, concomitant with downregulation and/or aberrant subcellular localization of two tumor-suppressor proteins E-cadherin and connexin-43. In addition, we demonstrate that epigenetic silencing of E-cadherin through promoter methylation is associated with neoplastic progression of our ovarian cancer model. These results establish critical interactions between cellular cytoskeletal remodeling and epigenetic silencing events in the progression of ovarian cancer. Thus, our MOSE model provides an excellent tool to identify both cellular and molecular changes in the early and late stages of ovarian cancer, to evaluate their regulation, and to determine their significance in an immunocompetent *in vivo* environment.

Neoplasia (2005) 7, 944–956

Keywords: E-cadherin, epigenetic silencing, promoter methylation, ovarian cancer, animal model.

It is the fourth leading cause of death among all cancers in women in Western countries and is the leading cause of death from female reproductive tract malignancies. Ovarian cancer is rarely diagnosed early, and reliable molecular or clinical markers to identify early changes have not been established. Moreover, prevention strategies that would inhibit early progression of this fatal disease are currently not available.

Most ovarian tumors originate from the surface epithelium lining and can be categorized into four major types: serous, endometrioid, mucinous, or clear cell tumors [2,3]. However, gene expression patterns only allow for the distinction of mucinous and clear cell carcinomas from serous tumors [4]. Human OSE cells are often found in the form of inclusion cysts and clefts, which may represent the earliest stage of neoplastic progression leading to primary ovarian tumors [2]. Dissemination of ovarian cancer cells into the peritoneal cavity is the result of the exfoliation of cells from the primary tumor. These cells can either form ascites containing tumor cell clusters, or migrate to distant sites throughout the peritoneum, where they will attach to the serosa and begin to form solid secondary tumors. The ability of ovarian tumor cells to adjust their migratory capacity requires reorganization in the actin cytoskeletal network (particularly at sites of focal adhesion complexes) and changes in cellular adhesion molecules, growth factor receptors, and intracellular signaling kinases [5,6]. These changes seem to be common events in an otherwise very heterogeneous disease.

Human OSE cells express epithelium-specific cytokeratins (mucins), display apical microvilli, but also express vimentin and N-cadherin, which are not typically expressed in epithelial cells [3,7]. Thus, OSE cells exhibit both mesenchymal and epithelial characteristics, an epithelial–mesenchymal phenotype. This mixed phenotype enables the OSE cells to respond rapidly

Introduction

Ovarian cancer is the deadliest gynecologic malignancy, with a survival rate of only 50%. In 2004, an estimated 25,500 women from the United States were diagnosed with—and 16,000 women died from—ovarian cancer [1].

Address all correspondence to: Paul C. Roberts, Department of Immunology/Microbiology, School of Medicine, Wayne State University, 7374 Scott Hall, 540 East Canfield Avenue, Detroit, MI 48201. E-mail: proberts@med.wayne.edu

¹This research was supported by the Elsa U. Pardee Foundation (P.C.R.) and the American Institute for Cancer Research (E.M.S.).

Received 17 May 2005; Revised 22 July 2005; Accepted 25 July 2005.

Copyright © 2005 Neoplasia Press, Inc. All rights reserved 1522-8002/05/\$25.00
DOI 10.1593/neo.05358

to a variety of environmental, hormonal, and stress factors, but is also thought to contribute to the onset of neoplastic transformation by rendering the cells more susceptible to transition from an epithelial to a mesenchymal-like phenotype [epithelial–mesenchymal transition (EMT)]. A deregulation of cellular adhesions and gap junctional intercellular communication (GJIC) has been described in the EMT of numerous types of epithelial-derived cancers (reviewed in Refs. [8,9]). E-cadherin expression in normal human ovarian surface epithelium is low to absent, but its expression, albeit variable, appears to increase in benign and many neoplastic stage I and II ovarian tumors, or in well-differentiated ovarian cancers [10–12]. E-cadherin expression is highly variable in advanced-stage ovarian carcinomas and is virtually undetectable in poorly differentiated ovarian cancer [12–15]. Mutational inactivation of E-cadherin is rare in ovarian cancers [16]. However, epigenetic silencing of E-cadherin gene expression through hypermethylation has been reported in cancers of other organs, including the bladder [17], breast, and prostate [18]. Similar to E-cadherin, downregulation of connexin-43 expression has been reported for advanced ovarian carcinoma [19]. Interestingly, suppression of GJIC by epigenetic silencing has been demonstrated in endometrial cancer [20].

Here, we report the establishment of a mouse ovarian cancer model representing the progressive stages of ovarian cancer. This model displays similar alterations in the actin cytoskeleton, cellular adhesion proteins, and connexin-43 that are observed in human ovarian cancer. Furthermore, we provide evidence that the downregulated expression of E-cadherin in cells representing the late stages of ovarian cancer is associated with the epigenetic silencing of its promoter region by DNA methylation. Thus, our syngeneic MOSE model derived from the C57BL/6 mouse represents an excellent *in vitro* and *in vivo* model used to characterize molecular and cellular events associated with ovarian carcinogenesis. Furthermore, immunotherapeutic strategies designed for the treatment of ovarian cancer can be evaluated in this syngeneic MOSE model.

Materials and Methods

Cell Culture

Mouse ovarian surface epithelial (MOSE) cells were isolated as described by Roby et al. [21]. Briefly, ovaries from female breeder mice (C57BL/6) were resected and, following removal of the residual remnants of the oviducts and bursa, were incubated for 20 minutes in Dulbecco's modified Eagle's medium (DMEM) supplemented with trypsin. Single cells and clumps of MOSE were collected, pelleted by mild centrifugation, resuspended in a MOSE growth medium, and seeded onto collagen-coated tissue culture dishes. The MOSE cell growth medium consisted of DMEM supplemented with 4% fetal bovine serum, 100 μ g/ml each of penicillin and streptomycin, 5 μ g/ml insulin, 5 μ g/ml transferrin, and 5 ng/ml sodium selenite (Invitrogen, Carlsbad, CA). During early passage of cells, the growth medium was further supplemented with mEGF (2 ng/ml) and hydrocortisone (0.5 μ g/ml). Collagen-coated flasks were discontinued after passage 5. Cells were

routinely passaged at a 1:6 to 1:12 ratio, depending on their growth rates. ID8 cells were generously provided by Drs. Paul F. Terranova and K. F. Roby (University of Kansas) [21].

For growth rate analyses, cells were seeded at densities of 1×10^4 and 5×10^4 cells, and subconfluent cell counts were determined at different times postseeding. Cell doubling times were estimated from the formula: $T \cdot \ln 2 / \ln(X_e/X_b)$, where X_e is the cell number determined at endpoint, X_b is the cell number at the beginning time point, and T is the total elapsed time (in hours).

To capture the cells in transitional states of carcinogenesis, we initially prepared frozen cell stocks after every five passages in cell culture. After passage 60, subsequent frozen stocks were prepared every 10 or 30 passages. In addition, we also prepared protein lysates and isolated RNA from select passages. The classification into early (MOSE-E), early/intermediate (MOSE-E/I), intermediate (MOSE-I), and late (MOSE-L) stages was based on ranges of passage number that displayed similar growth rates and anchorage-independent growth efficiencies, both in soft agar and in multicellular spheroid culture.

SKY Analysis

Cells were cultured for 2 days at 37°C. Mitotic cells were harvested then treated with colcemid for 2 hours. Chromosomal slides were prepared using the standard protocol, including hypotonic treatment, fixation, and air drying [22]. After pepsin treatment and fixation with formaldehyde followed by dehydration, the chromosomal slides were denatured and hybridized with denatured mouse painting probes (SkyPaint, Applied Spectral Imaging, Vista, CA) for over 48 hours at 37°C. Following postwash and detection, the chromosomes were stained with DAPI (4c6-diamidino-2-phenylindole-2HCl) and mounted with antifade. For each stage of cells, a total of 10 to 14 mitotic figures with good hybridization quality and minimal overlapping were captured using a charge-coupled device camera. This procedure was used for both the spectral and DAPI images [23]. Following image acquisition, chromosomes were karyotyped according to their color and size using Applied Spectral Imaging software [22,23].

Experimental Animals and Histopathology

Adult or 6- to 8-week-old female C57BL/6 mice were purchased from the Frederick Cancer Animal Research Production Laboratory of the National Institutes of Health (NIH). For *in vivo* tumor formation, mice were injected intraperitoneally with a total volume of 0.5 ml of phosphate-buffered saline (PBS) containing 5×10^6 cells of MOSE-E ($n = 3$) and MOSE-L ($n = 6$). As a positive control, we used ID8 cells ($n = 2$). Animals were weighed twice weekly and monitored for the development of ascites or palpable tumor formation for up to 60 days. All animal studies were approved by the Institutional Animal Care and Use Committee of the Wayne State University School of Medicine. At the time of sacrifice, organs were harvested and fixed in 10% buffered formalin. Routine paraffin embedding of tissues and hematoxylin and eosin staining of tissue sections were performed by AML Laboratories (Baltimore, MD).

Soft Agar Growth Assay and Matrigel Cultures

Cells (1.5×10^4) were suspended in 1.0 ml of 0.5% Bactoagar (Difco Laboratories, Detroit, MI) in the MOSE cell growth medium at 42°C, layered over 1 ml of 0.8% Bactoagar in DMEM in 12-well dishes, and cultured in 5% CO₂ in a humidified chamber. Colonies (>10 µm) were counted 10 to 21 days after seeding, and their size was determined using a $\times 10$ calibrated eyepiece. MOSE cell lines (2×10^4 cells/well) were also embedded directly in Matrigel diluted 1:1 with the growth medium. Following solidification of the Matrigel, cultures were incubated at 37°C with an overlay of growth medium and monitored over a 10-day period. Phase contrast images of colonies grown in Matrigel (BD Biosciences, Franklin Lakes, NJ) were captured with a Nikon Coolpix 990 digital camera attached to a Nikon Diaphot microscope using $\times 4$, $\times 10$, and $\times 20$ objectives. Alternatively, MOSE cells were cultured directly on Matrigel-coated 12-well dishes (Matrigel diluted 1:1 prior to coating) and incubated in growth medium at 37°C.

Spheroid Cultures

MOSE cells were seeded at a density of 1×10^5 cells/well in 12-well culture dishes coated with 1% agarose. Cells were gently agitated during the first several days of culture. Spheroid growth was monitored daily for a period of 7 to 14 days. Images of spheroids were digitally captured using a Nikon Coolpix 990 digital camera attached to an inverted Nikon Diaphot microscope using either a $\times 10$ or a $\times 20$ objective.

Collagen Raft Cultures

Organotypic collagen raft cultures were prepared essentially as described by Gregoire et al. [26], with minor modifications. Briefly, collagen plugs (2.5 ml of 1.63 mg/ml rat tail collagen; BD Biosciences) with or without fibroblast feeder cells were prepared in transwell filter inserts (BD Biosciences) and equilibrated with the MOSE cell growth medium prior to seeding cells. Cells (5×10^5) were seeded onto collagen plugs and allowed to grow to confluency at 37°C in a humidified incubator under 5% CO₂ for 1 to 2 days. Raft cultures were subsequently allowed to grow under an air/liquid interface for 14 to 21 days by removing the medium from the top chamber. We did not observe any influence of the fibroblast feeder cells on the growth properties of MOSE cells, so their use was discontinued. Cells were fed by changing the medium every 2 to 3 days from the bottom chamber. For histopathological analysis of the raft cultures, the cultures were overlain with 2% agarose in DMEM at 42°C and transferred to a 10% buffered formalin for processing by routine histopathology.

Western Blot Analysis

Cells grown in monolayer culture were scraped off the plates and lysed with RIPA buffer [10 mM Tris-HCl, 150 mM NaCl, 1% Triton X-100, 0.5% Na-deoxycholate, 0.1% sodium dodecyl sulfate (SDS), 1 mM EDTA, 0.2 mM PMSF, 1 µg/ml aprotinin, 1 µg/ml leupeptin, and 1 µg/ml pepstatin] for 30 minutes on ice. After passing through a 20-gauge needle (10 times), the lysates were centrifuged (15,000g) for 20 minutes at 4°C. Protein concentrations were determined

using a bicinchoninic acid protein assay kit (Pierce Biotechnology, Rockford, IL). Proteins (20–50 µg/lane) were separated on 10% or 12% SDS polyacrylamide gels and transferred to a PVDF membrane (BioRad, Hercules, CA). Membranes were blocked with 5% nonfat dry milk in Tris-buffered saline with Tween-20 (TBST containing 10 mM Tris, 150 mM NaCl, and 0.05% Tween-20, pH 8.0). Blots were immunostained using monoclonal antibodies for P-cadherin, E-cadherin, N-cadherin, connexin-43, phospho-connexin-43, vimentin, and p120catenin (BD Biosciences); β -catenin, vinculin and β -actin, and pan-cytokeratin (Sigma, St. Louis, MO); or polyclonal antibodies specific for mouse E-cadherin (R&D Systems, Inc., Minneapolis, MN), γ -catenin (or plakoglobin, sc-1497; Santa Cruz Biotechnology, Inc., Santa Cruz, CA), and vascular endothelial growth factor (VEGF; PC315; Oncogene, Cambridge, MA). Following incubation with appropriate horseradish peroxidase-conjugated secondary antibodies, proteins were visualized by enhanced chemiluminescence. A431 and rat cerebrum lysates (BD Transduction Laboratories) were used as positive controls. Densitometric quantitation of relative band intensity was performed using the NIH Image J program. Quantitation was normalized to relative optical units of β -actin or α -tubulin levels in each lane and expressed as a relative percent expression to the early passage of MOSE-E cells (MOSE-E set to 100%). Data are expressed as mean \pm standard deviation of two separate Western blot analyses using InStat (Graphpad Software, Inc., San Diego, CA).

Semiquantitative Reverse Transcription Polymerase Chain Reaction (RT-PCR)

Total RNA was extracted from cells using the Rneasy Mini Kit (Qiagen, Valencia, CA). First-strand synthesis was performed on 1 µg of total RNA and reverse-transcribed using the ImProm-II Reverse Transcription System (Promega, Madison, WI) and an oligo-dT primer, as per the manufacturer's instructions. Second-strand synthesis was performed on 0.75 µl of cDNA template using specific probes in a 15-µl PCR reaction volume using Qiagen Taq PCR Master Mix for 30 cycles at 94°C for 30 seconds, 60°C for 30 seconds, and 72°C for 45 seconds, with a final extension at 72°C for 7 minutes. Gene-specific primer sequences are available on request. PCR products were separated on 1.5% agarose gels and stained with ethidium bromide; gels were captured using the Eagle Eye II gel documentation system (Stratagene, La Jolla, CA). Band intensities were analyzed using the NIH Image J quantification software, expressed in arbitrary units. Expression levels were normalized to the relative expression of three housekeeping genes: β -actin, glyceraldehyde phosphate dehydrogenase (*GAPDH*), and phosphoglycerol kinase (*PGK*). Data were obtained by calculating the mean \pm SD of three separate PCRs using the statistics program InStat (GraphPad). PCR products were verified for the following size bands: β -actin, 138 bp; *GAPDH*, 168 bp; *PGK*, 366 bp; cyclin D1, 500 bp; β -catenin, 559 bp; connexin-43, 399 bp; E-cadherin, 376 bp; P-cadherin, 235 bp; N-cadherin, 508 bp; and VEGF isoforms, 345, 273, and 141 bp.

Methylation-Specific PCR (MSP)

Bisulfite modification of DNA was performed as previously described [24]. Briefly, 2 μ g of DNA was treated with sodium bisulfite (Sigma) for 16 hours at 50°C. Modified DNA was purified by passing through a QIAquick spin column (Qiagen) and eluting in 50 μ l of water. The reaction was completed by adding NaOH to a final concentration of 0.3 M for 5 minutes at room temperature (RT), followed by ethanol precipitation. DNA was resuspended in 25 μ l of water and stored at -20°C. MS-PCR was performed on 1 μ l of modified DNA in a 25- μ l reaction using the Qiagen Taq PCR Master Mix supplemented with MgCl₂ (final concentration, 6.8 mM). Methylation and unmethylation-specific primers were designed using MethPrimer [25]. The primer sequences of the promoter region of the mouse E-cadherin gene for the methylated reaction were 5'-GGTTGTCGTTTATTTTATAATCG-3' (sense) and 5'-AAACTTTAATCATCATCTAAATTCGGT-3' (antisense), and for the unmethylated reaction were 5'-GGTTGTTGTTTATTTTATAATTGG-3' (sense) and 5'-AAAACCTTAATCATCATCTAAATTTCCAT-3' (antisense). PCR conditions were 94°C for 5 minutes; 30 cycles of 94°C for 30 seconds, 62.5°C for 30 seconds, and 72°C for 45 seconds; and a final extension of 72°C for 7 minutes. A hot start was performed on the PCR reaction to aid in distinguishing methylated and unmethylated alleles. PCR products were separated on a 2% agarose gel and stained for ethidium bromide. For demethylation experiments, cells were treated with either 200 nM or 2 μ M 5'-aza-2'-deoxycytidine (5'-azaDC; Sigma) for 4 days and processed as described above.

Indirect Immunofluorescence Staining

Cells were grown on glass coverslips and fixed in either cold methanol (-20°C) or 3% paraformaldehyde followed by a permeabilization step in 0.5% Triton X-100 for 10 minutes at RT. Cells were blocked with 2% chicken serum for at least 60 minutes prior to immunostaining. Incubations with primary antibodies (see above) were carried out for 20 minutes at RT, followed by three to five washes with PBS. Appropriate secondary antibodies (chicken) conjugated to either AlexaFluor⁴⁸⁸, AlexaFluor⁵⁹⁴, or AlexaFluor⁶³⁵ (Molecular Probes, Eugene, OR) were carried out for 20 minutes at RT. Coverslips were mounted onto glass slides using Mowiol (Calbiochem, EMD Biosciences, La Jolla, CA). Immunofluorescence was observed using $\times 40$ and $\times 60$ objectives on a Nikon E800 epifluorescence microscope equipped with dual excitation and emission filter wheels, z-axis control, and a Coolsnap FX (Roper Scientific, Tucson, AZ) charge-coupled device camera. Images were captured and analyzed using Metamorph (Molecular Devices, Sunnyvale, CA) and Autoquant software (Autoquant Imaging, Inc., Troy, NY).

Results

Characterization of MOSE Cell Lines

To establish a syngeneic mouse cell model of ovarian cancer that represents distinct transitional states of neoplastic progression, we cultured normal primary MOSE cells,

which, on continued passage in cell culture, underwent spontaneous transformation and gradually progressed to a malignant phenotype. The malignant phenotype is defined by the ability to form colonies in soft agar, to grow as multicellular tumor nodules on organotypic raft culture, and to induce intraperitoneal tumor formation in the immunocompetent C57BL6 mouse.

Growth characteristics in monolayer, spheroid, organotypic collagen raft, and Matrigel cultures

As depicted in Figure 1, our MOSE model undergoes distinct phenotypic changes, which occur sequentially on continued passage in monolayer culture. Early-passage (MOSE-E) cells are larger, occupying two to three times the surface area of late-passage cells (Figure 1, *a* and *e*). They exhibit contact inhibition of growth and a typical epithelial cobblestone-like phenotype, characterized by well-defined cell-cell contact areas. MOSE-E/I cells are somewhat smaller and more heterogeneous, and there is evidence of acquisition of spindle-shape morphology in some of the cells when observed at a low seeding density (Figure 1, *b* and *f*). This transition to spindle-shape morphology progresses in intermediate-passage (MOSE-I) cells (Figure 1, *c* and *g*) and is the predominant phenotype in late-passage (MOSE-L) cells (Figure 1, *d* and *h*). In the latter two transitional states, cells are significantly smaller and do not exhibit contact inhibition of growth, which is evident by the formation of foci in the monolayer (arrows, Figure 1, *c* and *d*). All of the MOSE transitional cell types are cytokeratin-positive, confirming their epithelial-like origin. In addition, all cell lines were weakly positive for vimentin both by immunofluorescence staining and Western blot analysis (data not shown). At no time did we observe a loss of cytokeratin expression. This is reflective of the epithelial-mesenchymal phenotype of ovarian surface epithelium, which appears to be retained during MOSE progression.

To further demarcate these transitional states, we determined the growth rate and the capacity toward anchorage-independent growth, an *in vitro* hallmark of tumorigenic cell lines. The latter was assessed by the ability of the cells to grow as multicellular layers in an organotypic collagen raft or Matrigel culture, to form colonies in soft agar or Matrigel, as well as to grow as multicellular spheroids in suspension culture. As shown in Table 1, as cells make a transition to a more aggressive phenotype, their growth rates increase significantly, as has been described frequently in human cancer. During passaging, the cells progressively acquire the ability to invade and form multicellular layers on collagen rafts and grow as multicellular spheroids. The latter was highly dependent on passage number (Figure 1, *i-l*), with MOSE-L cells exhibiting spheroid growth greater than 200 μ m in diameter. The spheroids in MOSE-L cultures appeared to coalesce or fuse together, resulting in large, glandular-like spheroids. This was not observed in MOSE-I or MOSE-E/I cells, suggesting that malignant progression led to acquisition of this property. Interestingly, another mouse ovarian cancer cell line (ID8 cells) [21] did not display a capacity for multicellular spheroid growth and died after 6 days in spheroid culture (data not shown). A higher colony-forming efficiency (CFE) in soft

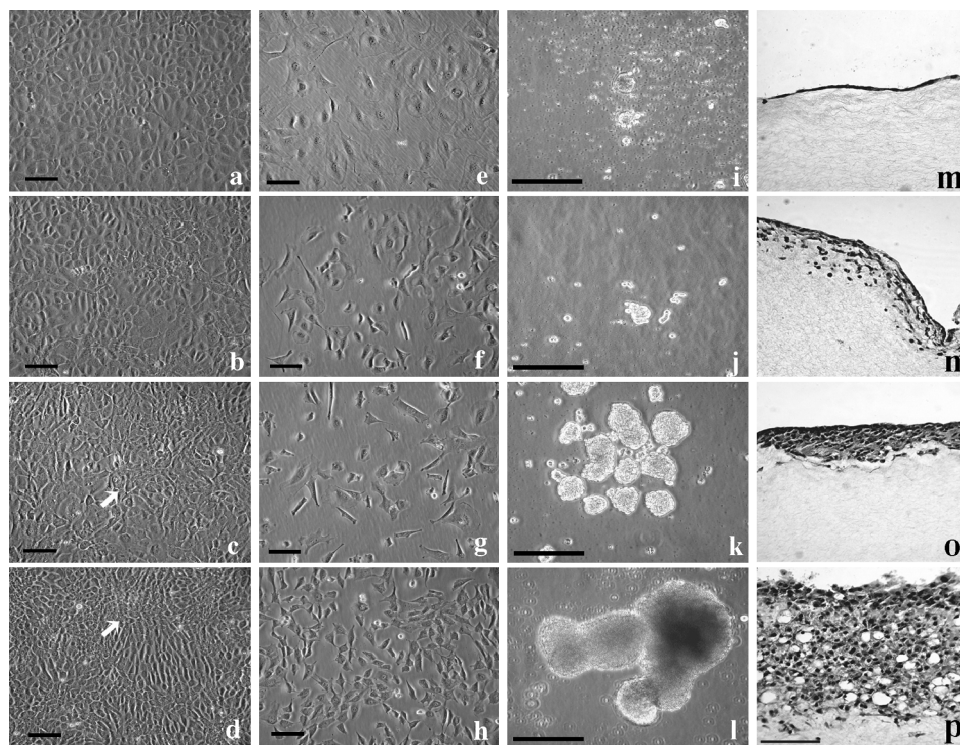


Figure 1. Cellular morphology of MOSE transitional cell lines in primary culture. MOSE-E (a, e, and i), MOSE-E/I (b, f, and j), MOSE-I (c, g, and k), and MOSE-L (d, h, and l) at confluent (a–d) and subconfluent (e–h) cell densities. Multicellular spheroids were cultivated for 7 days (i–l). Organotypic collagen raft cultures were cultivated for 14 days (m–p). Calibration bars, 100 μ m (a–h) and 200 μ m (i–l).

agar also appeared to be associated with an increasing passage number: CFE of MOSE-L>MOSE-I>MOSE-E/I>MOSE-E. Despite the lack of spheroid formation, ID8 cells were able to grow as colonies in soft agar (Table 1). In contrast to MOSE-E cells, which grow as a monolayer on collagen rafts, MOSE-E/I, MOSE-I, and MOSE-L cells progressively acquire the capacity to invade collagen and form multilayers (Figure 1, m–p). Interestingly, the growth phenotypes in organotypic raft culture closely mimic what we have previously reported for the neoplastic progression of E6/E7-immortalized human ovarian surface epithelial cells [26]. Concurrent with their increased growth rate and anchorage-independent phenotype, the MOSE-L cells also acquired the ability to grow aggressively and form vasculogenic-like structures when embedded in Matrigel (Figure 2B). In contrast, the early-passage MOSE-E cells only grew as small clusters of cells, confirming their low

tumorigenic potential (Figure 2A). When cells were cultured on top of Matrigel (data not shown), the MOSE-E cells grew as monolayers, which tended to roll up as sheets, whereas the MOSE-I and MOSE-L cells grew as multicellular aggregates, with the tendency to form vasculogenic-like structures similar to those depicted in Figure 2B. Interestingly, the vasculogenic-like protrusions displayed by MOSE-L grown in Matrigel (Figure 2B) were highly reminiscent of the structures observed during Matrigel cultures of highly aggressive human ovarian cancer cell lines [27].

In vivo growth properties of MOSE cells

The tumorigenic potential of our model was then confirmed *in vivo* in the immunocompetent C57BL6 mouse (Table 1). Female C57BL6 mice were injected intraperitoneally with 5×10^6 of MOSE-E or MOSE-L cells, and

Table 1. Growth Characteristics of MOSE Cell Lines.

MOSE Classification (Passage Number)	Doubling Rate (in Hours; \pm SEM)	% CFU* (\pm SEM)	Spheroid Growth [†]	Raft Culture [‡]	<i>In Vivo</i> Tumorigenicity [§]
MOSE-E p4–p15	26.51 (\pm 1.52)	0.4 (\pm 0.2)	±	S	0/3 mice
MOSE-E/I p20–p35	18.4 (\pm 0.95)	0.8–2.1 (\pm 0.4)	++	S/I	ND
MOSE-I p40–p80	15.55 (\pm 0.74)	2–5.4 (\pm 0.6)	+++	M/I	ND
MOSE-L p90–170	13.8 (\pm 0.51)	13.7–16 (\pm 1.1)	++++	M/I	6/6 mice (33–38 days)
ID8	15.08 (\pm 0.46)	11.8 (\pm 1.6)	±	M/I	2/2 mice (60 days)

E=Early; E/I=Early/Intermediate; I=Intermediate; and L=Late passage MOSE cells and passage range.

*Percent CFU (percent colony forming units in soft agar assay) = mean of the number of colonies per well/number of cells seeded per well \times 100.

[†]Spheroid growth defined as: (±) little to no growth; (++) spheroids < 50 μ m; (+++) spheroids > 50 < 200 μ m in diameter; and (+++++) spheroids > 200 μ m in diameter.

[‡]Organotypic collagen raft culture: S = single monolayer growth; I = invasion of collagen; and M = multilayered growth.

[§]Number of mice with detectable ascites or macroscopic evidence of peritoneal tumor formation. Days until death or sacrifice are reported in parenthesis.

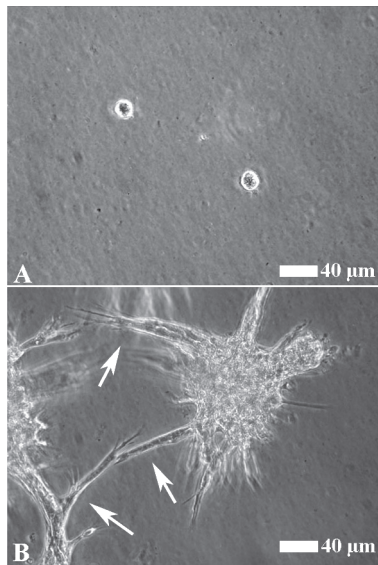


Figure 2. Aggressive growth phenotype assayed in Matrigel cultures. Suspensions of MOSE-E (A) and MOSE-L (B) cells were embedded in Matrigel and cultured at 37°C for up to 10 days. Digital micrographs recorded on day 5 postembedding are depicted. MOSE-E cells did not acquire the capacity to grow beyond a two- to six-cell cluster even at 10 days post-embedding. Vasculogenic-like structures emanating from MOSE-L cell clusters are indicated by arrows. Phase contrast images were recorded using a $\times 20$ objective.

formation of ascites or palpable tumors was followed for up to 60 days. We did not observe tumor formation or development of ascites in MOSE-E–injected mice. In contrast, mice injected with MOSE-L cells died after approximately 32 to 38 days. At necropsy, four of six mice showed massive tumor nodule formation throughout the abdominal cavity, with gastric outlet obstruction and a markedly distended stomach due to the tumor impinging on the pyloric/duodenal junction (Figure 3a); the remaining two mice showed peritoneal tumor nodule formation without gastric outlet obstruction. Lung consolidation was noted in five of six mice injected with MOSE-L cells and a few microscopic lymphangiectatic metastases. Hemorrhagic ascites were also present. Figure 3 shows a representative nodule of the poorly differentiated tumor, focally invading the pancreas (arrows, Figure 3b) and the pyloric/duodenal junction (arrows, Figure 3c).

Together, these *in vitro* and *in vivo* results demonstrate that we have indeed isolated different transitional states of MOSE cells as they progressed from a premalignant to a highly aggressive phenotype. We then investigated the underlying molecular changes associated with the neoplastic progression of MOSE cells.

SKY Analysis of MOSE Cells

To assess the degree of genomic instability in our MOSE cells, the cells were subjected to SKY analyses (summarized in Table 2). There were no clonal translocations detected at any stage tested. Nonclonal translocations were only detected in MOSE-L cells, albeit at low frequency. It is apparent that, even in the earliest transitional stage (MOSE-E), signifi-

cant genetic alterations have occurred (Table 2). The average chromosomal number observed in MOSE-E cells was 62. Even though 50% of cells at this stage displayed diploidy or near-diploidy ($40\pm$), only a few cells had completely normal karyotypes. The majority of the near-diploid cells displayed trisomy or monosomy, but as the cells progressed, there was a trend toward increased numeric abnormalities. Aneuploidy was highest in the intermediate-stage cells (MOSE-I), where the average chromosome number was 71; only 40% of cells at this stage were diploid or near-diploid, 50% of the cells were either near-triploid or tetraploid, and 10% displayed octaploidy. In the late-passage cells (MOSE-L), the average chromosome number was 60, with 30% displaying near-tetraploidy. One translocation occurred at this stage [$t(8;15)$]. It was not clonal aberration due to low frequency. There were no normal karyotypes among the cells displaying near-diploidy at this stage. Chromosomal loss was also observed during all stages, albeit at low frequency (10–20%).

Actin Reorganization during Malignant Transition

As cells make a transition from a normal to an aggressive cancer phenotype, epithelial cells must acquire the capacity

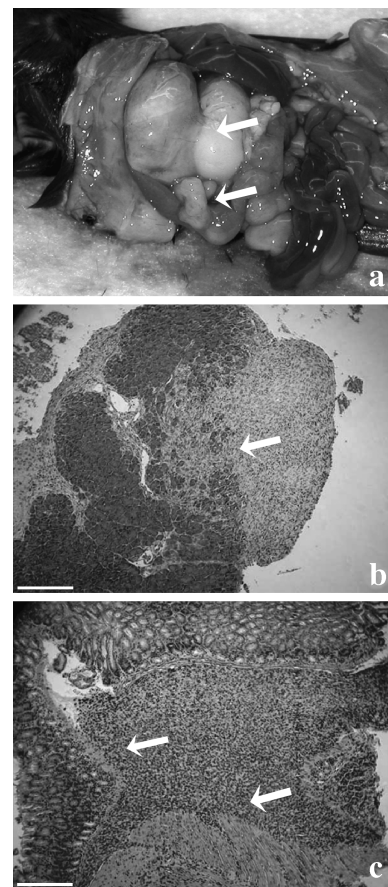


Figure 3. In vivo histopathology of MOSE-L cells. (a) Macroscopic image of a MOSE-L–injected C57BL6 mouse sacrificed at 35 days (arrows depict tumors and enlargement of the stomach). (b) Hematoxylin–eosin stain of tumor nodule on the pancreas, with arrows delineating invasion. (c) Hematoxylin–eosin stain of tumor invasion into the pyloric–duodenal junction. Calibration bar, 200 μ m.

Table 2. Summary of Chromosomal SKY Analysis of MOSE Transitional Stages.

MOSE Transitional Stages	Average Chromosome Number (Range)	Degree of Polyploidy (%)					
		Near-2N	Near-3N	Near-4N	Near-5N	Near-6N	Near-8N
E	62 (40–140)	50	30	10		10	
E/I	66 (40–86)	45	18	36			
I	71 (37–168)	40	20	30			10
L	60 (36–92)	60	10	30			

to migrate and invade different tissue types. During this transition, cells undergo drastic phenotypic changes, which are thought to primarily involve a reorganization of the cellular cytoskeleton and a deregulation of cellular adhesins and intercellular communication. Because of the role of F-actin and focal adhesion proteins, particularly vinculin, in maintaining the stability of the cytoskeleton and focal adhesion complexes, cytoskeletal reorganization events were monitored during the transitional progression of MOSE cells.

We assessed F-actin and vinculin organization in our model by indirect immunofluorescence staining (Figure 4). In early-passage cells (MOSE-E), prominent stress fibers and thick cortical actin ring structures were readily visualized by phalloiden staining (Figure 4, *a* and *c*). In addition, vinculin was observed to coalesce with F-actin at multiple adhesion plaques both at the cell periphery and at numerous cell–substratum contact areas (Figure 4, *b* and *d*). Vinculin-positive structures were elongated and terminated at the ends of actin bundles. Significant changes in F-actin and vinculin staining were not observed in MOSE-E/I cells. As cells progress to a more aggressive phenotype (MOSE-L cells; Figure 4, *e–h*), there is a concomitant loss or reduction in stress fiber formation, an increase in membrane ruffles, a reduction in cell–substratum vinculin staining, and smaller peripheral focal adhesion structures. Numerous phalloiden-positive projections emanating from the cell surface of MOSE-L cells were evident and were particularly prominent and extensive at cell–cell contact areas. These changes were evident in approximately 50% of MOSE-I cells (data not shown). These results indicate that both actin and focal adhesion remodeling are associated with the transitional progression of MOSE.

MOSE Cells Exhibit Differential mRNA and Protein Expression Profiles

One of the hallmarks of cancer progression is loss of functional adhesins and cytoskeletal remodeling, both of which may contribute to the metastatic potential of tumor cells. Because we observed actin remodeling as transition of the cells progressed, we postulated that the deregulation of adhesion complexes or GJIC may also be involved in the progression of MOSE cells. Thus, we determined the mRNA and protein expression profiles of several key cellular adhesion molecules (cadherins and associated catenins) and the gap junctional protein connexin-43. We also evaluated cyclin D1 and VEGF, which are known to be aberrantly expressed in human cancers.

Initially, we examined mRNA expression profiles by semi-quantitative RT-PCR (Figure 5, *A* and *B*). To minimize the effects of a potential aberrant expression of housekeeping genes, we normalized all expression levels to three different housekeeping genes: β -actin, GAPDH, and PGK. In our panel of selected genes, which includes *E-cadherin*, *N-cadherin*, *P-cadherin*, β -catenin, *plakoglobin*, *connexin-43*, *cyclin D1*, and *VEGF*, only *E-cadherin* mRNA was significantly down-regulated in our model. The loss of *E-cadherin* mRNA expression followed the transitional progression of the MOSE cells, with MOSE-I and MOSE-L cells exhibiting significant decreases in *E-cadherin* mRNA expression. *Cyclin D1* was the only gene in our panel that was upregulated early during the transition of MOSE-E to MOSE-E/I. *P-cadherin*, *plakoglobin*, and *VEGF* mRNA (data not shown), or *N-cadherin*,

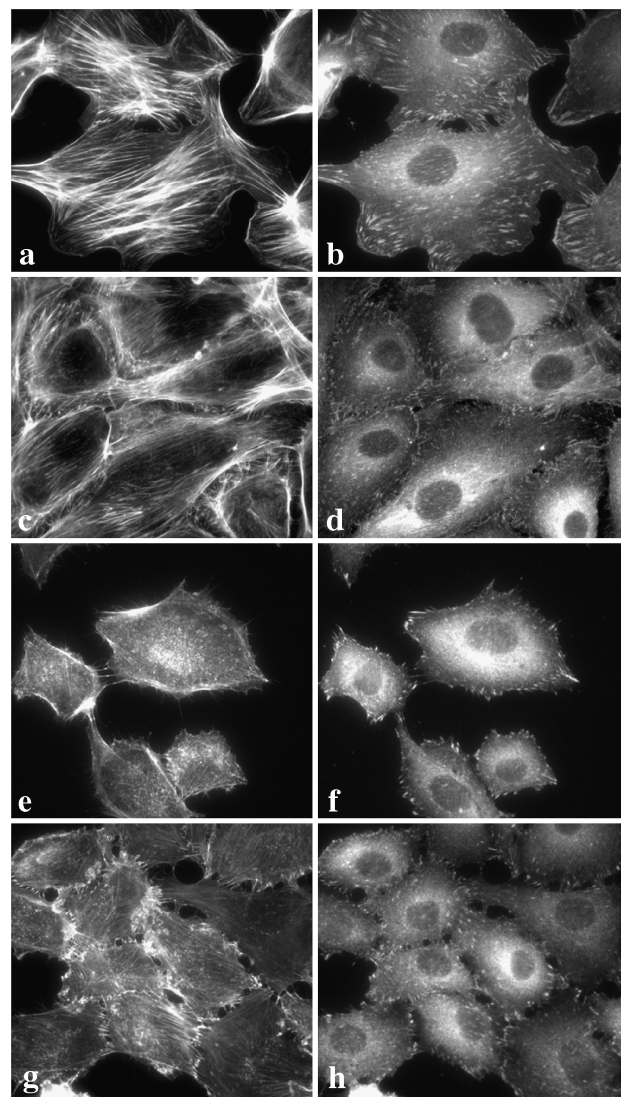


Figure 4. Actin reorganization and reduction in focal adhesion plaques in MOSE cells. Immunofluorescent staining of MOSE-E (*a–d*) and MOSE-L (*e–h*) with AlexaFluor⁴⁸⁸ phalloiden to visualize F-actin was performed on cells seeded at both low (*a* and *e*) and high seeding densities (*c* and *g*). Vinculin staining (*b*, *d*, *f*, and *h*) of the same cells with monoclonal mouse anti-vinculin antibody and AlexaFluor⁵⁹⁴-conjugated chicken antimouse Ig (original magnification, $\times 600$).

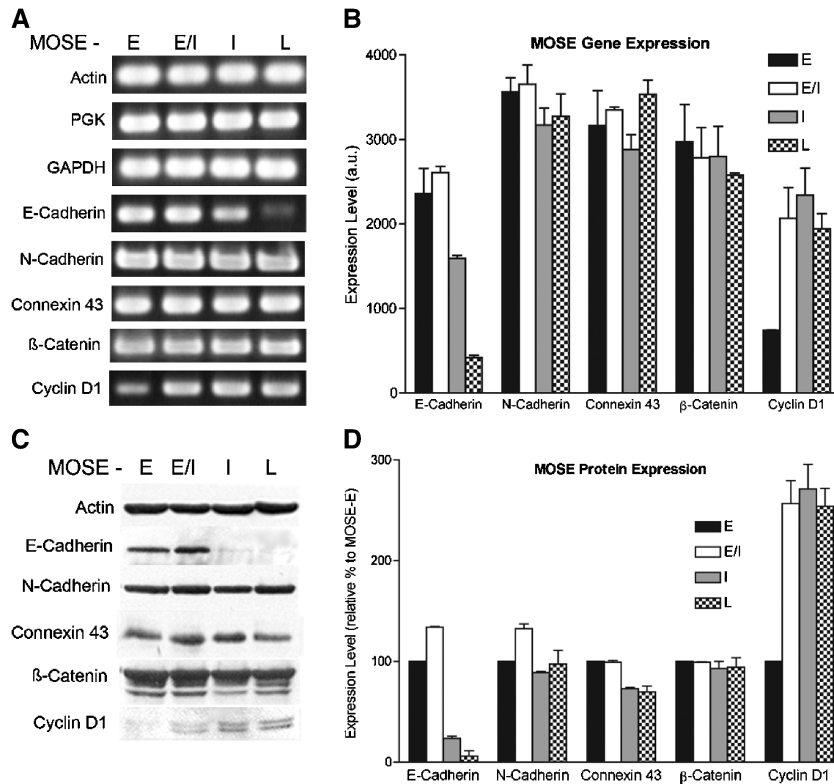


Figure 5. Differential mRNA and protein expression profiles during MOSE neoplastic progression. (A) Representative mRNA expression profile of MOSE cell lines by semiquantitative RT-PCR. (B) Relative expression levels of selected genes normalized to the three housekeeping genes β -actin, PGK, and GAPDH. (C) A representative protein expression profile of selected proteins by Western blot analysis. (D) Relative protein expression levels compared to levels in MOSE-E cells.

connexin-43, and β -catenin were detected at comparable levels across all transitional states of MOSE cells.

In parallel, we also determined protein expression profiles by Western blot analysis. As depicted in Figure 5, C and D, protein levels of N-cadherin and β -catenin did not change significantly during the malignant transition of MOSE cells. In agreement with the mRNA profiles, protein levels of cyclin D1 were elevated early in our model. In contrast, E-cadherin protein levels decreased in later stages. Using immunohistochemistry, we also evaluated E-cadherin expression *in vivo* in tumor tissues from MOSE-L-injected mice (data not shown). Here, E-cadherin expression was weak and predominantly cytoplasmic when compared to control mouse tissue derived from colonic and breast epithelium. Thus, the loss of E-cadherin is a stable phenotype of MOSE-L cells. Significant protein level changes in connexin-43, P-cadherin (weakly present in all cell lines), VEGF, or plakoglobin were not observed (data not shown).

Subcellular Localization of E-cadherin and Connexin-43 Is Altered during Malignant Progression of MOSE

Aberrant subcellular localization of tumor-suppressor proteins—in addition to, or instead of, altered expression—can contribute to malignant progression. Hence, we asked whether subcellular localization of the cadherins, catenins, and connexin-43 proteins was altered during the transitional progression of MOSE cells. This was particularly important with respect

to β -catenin in light of the downregulated expression of E-cadherin. The association of both proteins at junctional complexes is thought to be strictly regulated to limit the appearance of cytosolic and nuclear β -catenin that are commonly associated with changes in proliferation and adhesion in the early stages of cancer.

Comparative immunofluorescence staining of transitional MOSE cell lines revealed distinct differences both in the localization and relative amounts of the cellular adhesion molecule E-cadherin and the gap junctional complex protein connexin-43. During early stages, both β -catenin and E-cadherin immunostainings colocalized to the periphery at cell–cell junctions (Figure 6, a–c). As cells progressed to a more malignant, aggressive phenotype, the percentage of cells exhibiting positive E-cadherin staining gradually decreased from 90% to 100% in MOSE-E and MOSE-E/I to less than 30% of MOSE-I (Figure 6, d–f) and 0% of MOSE-L (Figure 6, g–i). Interestingly, loss of peripheral E-cadherin did not change the expression of catenins present at the periphery because β -catenin, plakoglobin, and p120 catenin (Figure 6, g–i; data not shown) were present at the cell periphery. Subsequent immunostaining revealed that N-cadherin is the predominant peripheral cadherin present in all transitional states of MOSE cells (data not shown).

Although mRNA and protein levels of connexin-43 were maintained during neoplastic progression, subcellular localization changed dramatically. In the early stages of our model, connexin-43 was largely restricted to cell–cell contact areas,

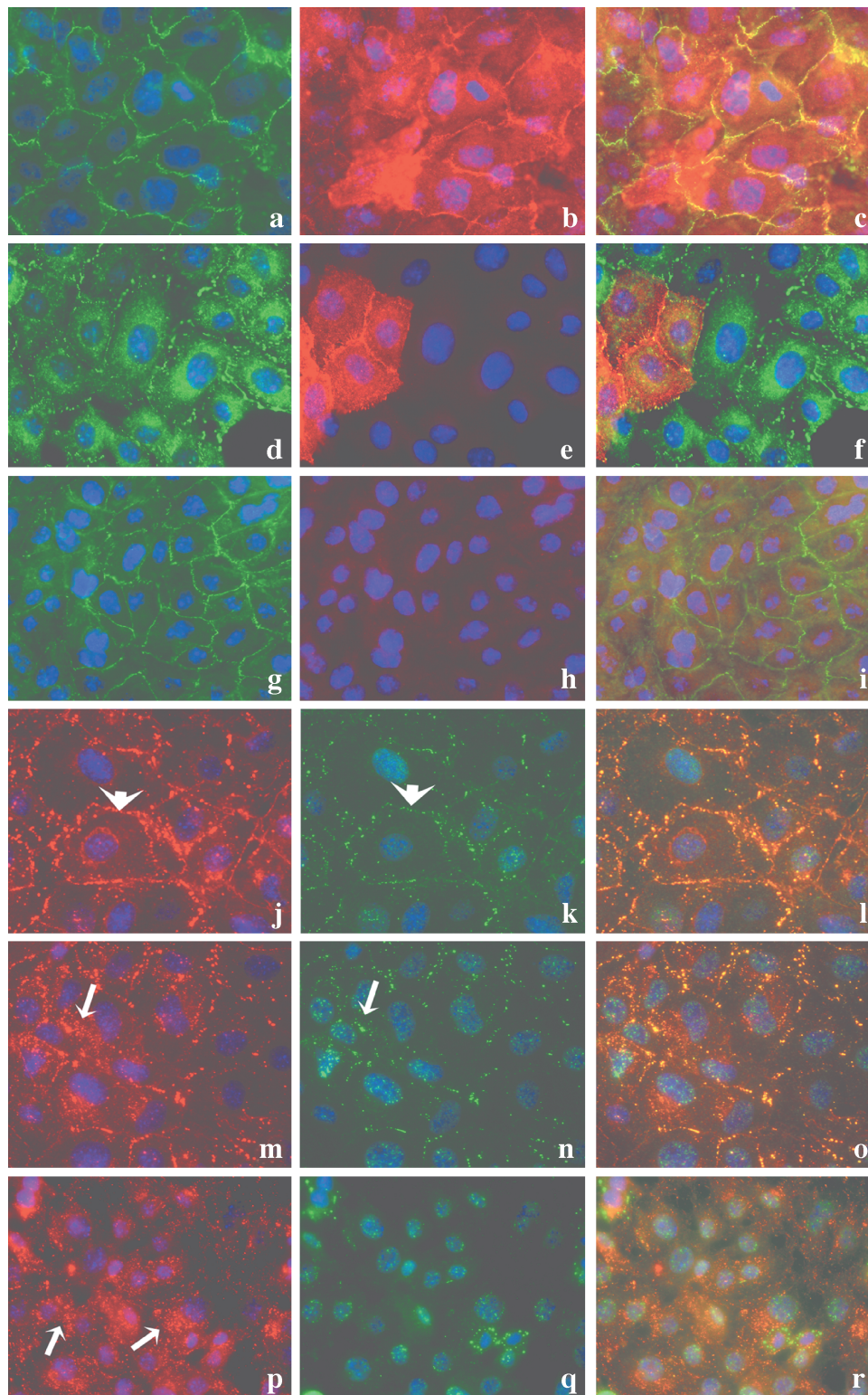


Figure 6. Aberrant subcellular localization of E-cadherin and connexin-43 in MOSE transitional cells. Upper panels (a–i): Dual immunofluorescence staining of MOSE-E (a–c), MOSE-I (d–f), and MOSE-L cells (g–i) depicting β -catenin (green), E-cadherin (red), and DAPI staining (blue). Colocalization is visualized by yellow staining in merged images (c, f, and i) (original magnification, $\times 600$). Lower panels (j–r): Immunofluorescent localization of connexin-43 (red), phosphorylated connexin-43 (green), and DAPI (blue) in MOSE-E (j–l), MOSE-I (m–o), and MOSE-L cells (p–r). Yellow staining in merged images (l, o, and r) depicts colocalization. Arrowheads in (j) and (k) delineate gap junctional plaque regions; arrows in (m) and (n) indicate intracellular aggregates of connexin-43 (original magnification, $\times 600$).

where it coalesced into discrete punctate plaques at junctional sites along the cell periphery (Figure 6, j–l). Double immuno-

fluorescence staining with a phospho-specific connexin-43 antibody confirmed that the connexin-43 at gap junctional

plaques was partially phosphorylated (Figure 6*k*). In contrast, more advanced stages exhibited reduced connexin-43 junctional plaques, and staining became prominent in intracellular compartments (Figure 6, *m–r*). Connexin-43–positive staining in these intracellular compartments colocalized with NBD-C6 ceramide staining, but did not colocalize with antibodies against EE1, an early endosomal compartment antigen, or with LysoTracker-RED (data not shown), suggesting that connexin-43 transport in late-passage MOSE cells is restricted to a Golgi-like compartment. Immunostaining with the phospho-specific connexin-43 antibody failed to reveal any subcellular difference, suggesting that altered phosphorylation was not responsible for the failure of the cells to transport connexin-43 to junctional regions. It should be noted that there were residual patches of cells in MOSE-L cultures that did display normal connexin-43 at junctional plaques, suggesting that, despite the loss of E-cadherin, a subset of MOSE-L cells retains the capacity for normal connexin-43 trafficking.

Epigenetic Silencing of the E-cadherin Gene by Hypermethylation

Recently, efforts have focused on the role of hypermethylation in the epigenetic gene silencing of tumor-suppressor genes [28]. Due to the downregulation of E-cadherin mRNA and protein levels (5- and 10-fold, respectively), we asked whether methylation of the CpG islands in the mouse E-cadherin promoter region could be partially responsible for the silencing of the E-cadherin gene as transition of the MOSE cells progressed. Initially, we assessed the ability of the potent DNA methyltransferase inhibitor, 5'-aza-2'-deoxycytidine (5'-azaDC), to overcome the repression of the mRNA synthesis of the E-cadherin gene. As revealed by RT-PCR, an increase in E-cadherin mRNA levels was achieved by the treatment of MOSE-L cells with 5'-azaDC (Figure 7*A*). To determine if E-cadherin promoter methylation is associated with progression in our cancer model, we performed MSP on bisulfite-treated DNA derived from different transitional states. As

depicted in Figure 7*B*, MOSE-E cells displayed partial methylation as evidenced by the presence of both methylated and unmethylated PCR amplicons, but the unmethylated species appeared to be the predominant form (band ratio of methylated to unmethylated, M:U = 0.7). As cells make a transition, there is a gradual loss of the unmethylated species and a concomitant increase in the methylated species (M:U = 1.4, MOSE-E/I; M:U = 3.2, MOSE-I; and M:U = 10, MOSE-L). Mouse ovarian stromal fibroblasts (OSFs) that do not express E-cadherin protein or mRNA serve as unmethylated controls (Figure 7*C*). Importantly, E-cadherin promoter methylation is a reversible process in our model because treatment with 5'-azaDC (Figure 7*D*) can partially convert the methylated form to an unmethylated form (M:U = 1.2). Together, these results demonstrate that gene silencing through methylation occurs during the malignant progression of MOSE cells and that this is an early and reversible effect, thereby identifying promoter gene methylation as a target for anticancer agents.

Discussion

Various cell models have been developed to study OSE cells, but cell culture models that allow for delineation of transitional states of ovarian carcinogenesis both *in vitro* and *in vivo* have not been well established. Because of the very slow rate of spontaneous transformation in human ovarian cells, we and others have employed SV40, human papillomavirus E6/E7, Ras, or hTERT transduction to induce the immortalization or transformation of cultured human OSE cells [26,29–31]. Genetically modified adenoviruses have been used to illustrate that inactivation of both p53 and RB1 leads to induction of tumorigenesis in the mouse [32]. More recently, a mouse ovarian cancer model using genetically engineered mice expressing the SV40 T antigen under the control of the MSIIR promoter has been described [33]. A rat model of spontaneous ovarian tumor progression has provided interesting insights into progressive cytogenetic changes during tumorigenesis [34,35]. However, these cells

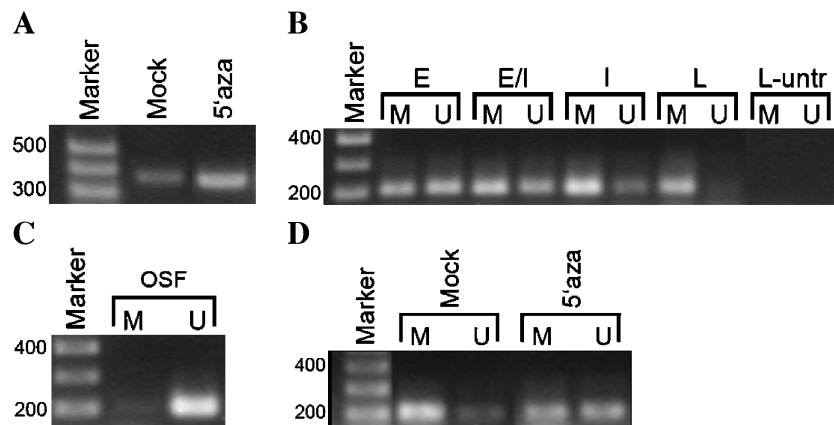


Figure 7. The mouse E-cadherin promoter region undergoes transitional methylation in MOSE cells. (A) RT-PCR analysis of E-cadherin mRNA in MOSE-L cells treated in the presence or absence of 5'-azaDC. (B) MS-PCR of bisulfite-treated DNA derived from MOSE-E, MOSE-E/I, MOSE-I, and MOSE-L cells with primer sets specific for either the unmethylated (U) or methylated (M) CpG islands in the mouse E-cadherin promoter region. Untreated MOSE-L DNA (L-untr) was used as a negative control for MSP-PCR. (C) MS-PCR of bisulfite-treated DNA derived from mouse OSF cells as a nonmethylated control. (D) MS-PCR of bisulfite-treated DNA derived from MOSE-L cells treated with or without 5'-azaDC.

quickly become malignant and already form tumors after 6 to 10 passages, leaving only a very short time frame for the molecular analysis of tumor biology and intervention. Initiation of ovarian cancer in rats with DMBA provided a model for chemically induced ovarian cancer, but cell lines for a rapid screening of chemopreventive/therapeutic compounds *in vitro* were not isolated and characterized [36].

In other existing rodent models, human cancer cells are used as xenografts in immunodeficient mice. These models lack critical site-specific interactions between tumor and stromal cells, or regulatory stimuli from the immune system. This is especially critical because ovarian cancer is a disease of older women, and changes in the immune response (termed *immunosenescence*) have been implied in the cancer of the ovaries and other cancers [37]. These already existing models provide important insights into ovarian tumor biology, but may or may not be representative of the heterogeneous and spontaneous nature of human ovarian cancer. However, established cell lines represent only a limited number of advanced human ovarian tumors in their genetic makeup.

In the present study, we have isolated and identified transitional states of ovarian cancer as normal mouse OSE cells spontaneously undergo neoplastic transformation during culturing. It was our goal to establish a model system representing early, intermediate, and late stages of ovarian cancer that can be used for *in vitro* mechanistic studies, as well as for efficacy studies *in vivo* of both chemotherapeutic treatment regimens and chemopreventive strategies in immunocompetent mice. This is significant because it enables us to include stromal constituents and immune surveillance in the studies of progression of ovarian cancer, a limiting factor in studies in nude mice with xenografts of human or rat ovarian cell lines. In our model, a minimum of four transitional states were distinguishable by *in vitro* growth criteria, which included growth rate, CFE in soft agar, ability to form multicellular spheroids or vasculogenic-like structures in Matrigel, and morphologic phenotypes as determined by cell size and actin and focal adhesion organization. In addition, *in vivo* tumorigenicity was confirmed in syngeneic immunocompetent mice. MOSE-E cells represent the earliest transitional state of our model, characterized by a slow growth rate, contact inhibition of growth, inability for anchorage-independent growth, and failure to induce tumor formation in syngeneic mice. This stage—albeit not normal—displays many characteristics reminiscent of normal human OSE cells, including correctly localized connexin-43, cadherins, and catenins. In addition, it exhibits an actin cytoskeleton that promotes and favors strong cell–substratum as well as cell–cell attachments. Furthermore, cells at this stage grow as a single monolayer in organotypic raft culture and on Matrigel, reminiscent of normal ovarian surface epithelium. However, the MOSE-E stage has already clearly undergone significant genetic changes as indicated by the SKY analysis; in the majority of near-diploid cells, monosomy and trisomy were observed. Thus, the early MOSE-E stage represents an excellent model for early preneoplastic ovarian cancer, which has not yet obtained the changes necessary to elicit tumor formation *in vivo*.

MOSE-L cells represent the most aggressive transitional stage: rapid growth rate, enhanced capacity for anchorage-independent growth, and rapid tumorigenic potential *in vivo*. These characteristics are associated with a disorganized actin cytoskeleton and reduced focal adhesions concurrent with the aberrant localization of connexin-43 and the down-regulation of E-cadherin gene expression. Many of the clinical features typical of ovarian cancer, including the presence of tumor nodules throughout the omentum, gastric outlet obstruction, and lymphangiectatic metastasis in the lungs, were recapitulated in our model, as was the formation of hemorrhagic ascites. We did not observe major chromosome structural abnormalities in this mouse model; however, progressive aneuploidy was observed as the cells transitioned to a more aggressive phenotype. This is in agreement with the karyotypic analysis of the cell lines generated by Roby et al. [21], in which the most common occurrence was tetraploidy in aggressive cell lines. The progressive increase in polyploidy that we observed in the transition from MOSE-E to MOSE-I has also been reported in human ovarian cancer [38]. The lack of major structural aberrations on chromosomes, but an increase in numeric alterations, may be inherent to the mouse model. Increased structural alterations may also be a characteristic associated with the heterogeneity of *in vivo*-derived tumor tissue. Alternatively, our MOSE cells may represent an earlier stage of progression than that characterized in human primary ovarian carcinomas. Future studies are planned to address the genomic stability of our cells *in vivo*.

E-cadherin appears to be minimally expressed or completely absent in normal human OSE cells, but has been observed in inclusion cysts and cleft formations in the normal ovary [12,13,39]. Normal mouse OSE cells have been reported to express E-cadherin [40], which may be reflective of a more mature, differentiated state in MOSE cells [2]. In contrast, metaplastic and early stages of ovarian cancer do express variable levels of E-cadherin [39]. However, loss of E-cadherin likely contributes to metastatic potential in late-stage ovarian carcinoma [12,41,42]. The loss of E-cadherin expression is frequently associated with the EMT. Its re-expression partially leads to the reverse transitional step, MET [42]. The sometimes contradictory reports of E-cadherin expression in ovarian cancer are likely due to the epithelial–mesenchymal mixed origin of OSE cells, which allows them to naturally revert back and forth between EMT or MET. Loss of E-cadherin expression due to mutational inactivation is a rare event in ovarian cancer [16]. Consistent with observations in human disease, we find a slightly upregulated E-cadherin expression in early stages, followed by a reduction and silencing of E-cadherin expression in the late stages of our mouse ovarian cancer model. The loss of E-cadherin expression was associated with an increased methylation of the promoter region, resulting in gene silencing. Promoter hypermethylation is a well-documented regulatory event associated with neoplastic progression of multiple types of cancer (see Ref. [43]). Our results clearly demonstrate that methylation of the promoter region of the mouse E-cadherin gene increases during neoplastic transition of MOSE, resulting

in reduced mRNA and protein expression, which can be partially restored by treatment with 5'-azaDC. Global hypermethylation of CpG islands appears to be prevalent but variable in ovarian cancer tissue [44–46]; hence, we expect that other genes would also be differentially methylated in our MOSE model. Future studies using microarray analyses for a more global expression profiling will help identify other marker genes undergoing methylation-induced gene silencing in this model.

Downregulation of E-cadherin did not result in altered localization of β -catenin, which was still found at the periphery and colocalized with plakoglobin and N-cadherin, regardless of the transitional stage of MOSE. Thus, in normal and malignant MOSE, N-cadherin and probably P-cadherin can serve as anchors for β -catenin at junctional complexes, thereby preventing aberrant cytosolic or nuclear accumulation of β -catenin. Normal human OSE cells have also been shown to express N-cadherin [11,47]. A recent study has suggested that E-cadherin, N-cadherin, and P-cadherin are differentially expressed during the neoplastic progression of OSE cells [11]. This concept of “cadherin switching” set forth by Patel et al. [11] may partially explain the ability of the ovarian cancer cell to micromanage itself in response to the cellular environment, facilitating both motility and adhesion to multiple surfaces or tissues.

GJIC is essential for tissue homeostasis and helps regulate cell proliferation, apoptosis, and differentiation. In general, GJIC appears to be disrupted in malignant cells, allowing cells to escape growth constraints that are typically imposed by neighboring cells, leading to clonal expansion and subsequent tumor formation [48]. Connexin-43 has been shown to be significantly reduced in human ovarian carcinoma or established cell lines, compared to normal OSE cells [19,49]. Forced expression of connexins can lead to a partial reversion of the malignant phenotype [50,51]. In our MOSE model, connexin-43 mRNA and protein levels were not affected. However, the subcellular distribution of connexin-43 was severely altered during the neoplastic progression of MOSE. This is important because *in vitro* inhibition of neoplastic cell growth by coculture with nontransformed cells has been shown to require functional GJIC [52]. Our results support a role of aberrant connexin-43 localization with a neoplastic transition of the ovarian surface epithelium, but also emphasize the need to corroborate global gene expression profile data with subcellular distribution profiles of the corresponding proteins.

It should be noted that there appears to be a close link between gap junctional intercellular crosstalk and crosstalk initiated by E-cadherin. In endometrial cancer cells, gap junctional communication was found to be suppressed when the E-cadherin gene was silenced by hypermethylation [20]. In murine skin papilloma cells, intracellular trafficking of connexins was dependent on E-cadherin expression [53]. Interestingly, in the latter study, the presence of E-cadherin at junctional complexes appeared to be required for the formation of actin stress fibers, which facilitate the transport of connexins to the cell surface. This would partially explain the transitional state of the MOSE-L cells, where we observed

a lack of actin stress fibers, intracellular accumulation of connexin-43, and loss of E-cadherin gene expression. It is also evident from our observations that N-cadherin expression and proper trafficking may compensate for the loss of E-cadherin and may serve to target connexin-43 to gap junctional plaques. Patches of cells in MOSE-L cultures that were E-cadherin-negative but N-cadherin-positive did display connexin-43 at junctional plaques.

In summary, we have established a syngeneic mouse ovarian cancer cell model that differentiates between the early, early/intermediate, intermediate, and late stages of ovarian cancer. In our model, we observed progressive alterations in cytoskeletal, adhesion, and intercellular communication proteins typically seen in human ovarian cancer. Thus, our model can be used to study the mechanisms of neoplastic progression both *in vitro* and *in vivo*. Importantly, *in vivo* analysis can be conducted in the immunocompetent mouse, allowing for an evaluation of immune surveillance in ovarian carcinogenesis. This model will also be useful for the evaluation of both chemopreventive and chemotherapeutic treatment regimens, providing multiple stages and intracellular proteins as markers for treatment efficacy. Perhaps the most exciting use of this new model is in probing gene expression changes during early stages of ovarian tumorigenesis. Both the MOSE-E and MOSE-E/I stages should provide new insights into genes involved in neoplastic progression and new targets for prevention and treatment efforts.

Acknowledgements

We are indebted to L. Polin (Karmanos Cancer Institute) for technical advice with the animal studies. We kindly thank M. A. Tainsky (Karmanos Cancer Institute) for critically reading the manuscript.

References

- [1] Jemal A, Tiwari RC, Murray T, Ghafoor A, Samuels A, Ward E, Feuer EJ, and Thun MJ (2004). Cancer statistics, 2004. *CA Cancer J Clin* **54** (1), 8–29.
- [2] Auersperg N, Ota T, and Mitchell GW (2002). Early events in ovarian epithelial carcinogenesis: progress and problems in experimental approaches. *Int J Gynecol Cancer* **12** (6), 691–703.
- [3] Sundfeldt K (2003). Cell–cell adhesion in the normal ovary and ovarian tumors of epithelial origin; an exception to the rule. *Mol Cell Endocrinol* **202** (1–2), 89–96.
- [4] Schwartz DR, Kardias SL, Shedden KA, Kuick R, Michailidis G, Taylor JM, Misek DE, Wu R, Zhai Y, Darrah DM, et al. (2002). Gene expression in ovarian cancer reflects both morphology and biological behavior, distinguishing clear cell from other poor-prognosis ovarian carcinomas. *Cancer Res* **62** (16), 4722–4729.
- [5] Bast RC Jr, Boyer CM, Jacobs I, Xu FJ, Wu S, Wiener J, Kohler M, and Berchuck A (1993). Cell growth regulation in epithelial ovarian cancer. *Cancer* **71** (Suppl 4), 1597–1601.
- [6] Cruet S, Salamanca C, Mitchell GW, and Auersperg N (1999). α v β 3 and vitronectin expression by normal ovarian surface epithelial cells: role in cell adhesion and cell proliferation. *Gynecol Oncol* **75** (2), 254–260.
- [7] Auersperg N, Wong AS, Choi KC, Kang SK, and Leung PC (2001). Ovarian surface epithelium: biology, endocrinology, and pathology. *Endocr Rev* **22** (2), 255–288.
- [8] Thiery JP (2002). Epithelial–mesenchymal transitions in tumour progression. *Nat Rev Cancer* **2** (6), 442–454.
- [9] Chipman JK, Mally A, and Edwards GO (2003). Disruption of gap junctions in toxicity and carcinogenicity. *Toxicol Sci* **71** (2), 146–153.

- [10] Auersperg N, Edelson MI, Mok SC, Johnson SW, and Hamilton TC (1998). The biology of ovarian cancer. *Semin Oncol* **25** (3), 281–304.
- [11] Patel IS, Madan P, Getsios S, Bertrand MA, and MacCalman CD (2003). Cadherin switching in ovarian cancer progression. *Int J Cancer* **106** (2), 172–177.
- [12] Davies BR, Worsley SD, and Ponder BA (1998). Expression of E-cadherin, alpha-catenin and beta-catenin in normal ovarian surface epithelium and epithelial ovarian cancers. *Histopathology* **32** (1), 69–80.
- [13] Sundfeldt K, Piontek Y, Ivarsson K, Nilsson O, Hellberg P, Brannstrom M, Janson PO, Enerback S, and Hedin L (1997). E-cadherin expression in human epithelial ovarian cancer and normal ovary. *Int J Cancer* **74** (3), 275–280.
- [14] Peralta Soler A, Knudsen KA, Tecson-Miguel A, McBrearty FX, Han AC, and Salazar H (1997). Expression of E-cadherin and N-cadherin in surface epithelial–stromal tumors of the ovary distinguishes mucinous from serous and endometrioid tumors. *Hum Pathol* **28** (6), 734–739.
- [15] Darai E, Scoazec JY, Walker-Combrout F, Mlika-Cabanne N, Feldmann G, Madelenat P, and Potet F (1997). Expression of cadherins in benign, borderline, and malignant ovarian epithelial tumors: a clinicopathologic study of 60 cases. *Hum Pathol* **28** (8), 922–928.
- [16] Risinger JI, Berchuck A, Kohler MF, and Boyd J (1994). Mutations of the E-cadherin gene in human gynecologic cancers. *Nat Genet* **7** (1), 98–102.
- [17] Ribeiro-Filho LA, Franks J, Sasaki M, Shiina H, Li LC, Nojima D, Arap S, Carroll P, Enokida H, Nakagawa M, et al. (2002). CpG hypermethylation of promoter region and inactivation of E-cadherin gene in human bladder cancer. *Mol Carcinog* **34** (4), 187–198.
- [18] Graff JR, Herman JG, Lapidus RG, Chopra H, Xu R, Jarrard DF, Isaacs WB, Pitha PM, Davidson NE, and Baylin SB (1995). E-cadherin expression is silenced by DNA hypermethylation in human breast and prostate carcinomas. *Cancer Res* **55** (22), 5195–5199.
- [19] Hanna EA, Umhauer S, Roshong SL, Piechocki MP, Fernstrom MJ, Fanning JD, and Ruch RJ (1999). Gap junctional intercellular communication and connexin43 expression in human ovarian surface epithelial cells and ovarian carcinomas *in vivo* and *in vitro*. *Carcinogenesis* **20** (7), 1369–1373.
- [20] Nishimura M, Saito T, Yamasaki H, and Kudo R (2003). Suppression of gap junctional intercellular communication via 5' CpG island methylation in promoter region of E-cadherin gene in endometrial cancer cells. *Carcinogenesis* **24** (10), 1615–1623.
- [21] Roby KF, Taylor CC, Sweetwood JP, Cheng Y, Pace JL, Tawfik O, Persons DL, Smith PG, and Terranova PF (2000). Development of a syngeneic mouse model for events related to ovarian cancer. *Carcinogenesis* **21** (4), 585–591.
- [22] Heng HH, Liu G, Lu W, Bremer S, Ye CJ, Hughes M, and Moens P (2001). Spectral karyotyping (SKY) of mouse meiotic chromosomes. *Genome* **44** (2), 293–298.
- [23] Ye CJ, Lu W, Liu G, Bremer SW, Wang YA, Moens P, Hughes M, Krawetz SA, and Heng HH (2001). The combination of SKY and specific loci detection with FISH or immunostaining. *Cytogenet Cell Genet* **93** (3–4), 195–202.
- [24] Herman JG, Graff JR, Myohanen S, Nelkin BD, and Baylin SB (1996). Methylation-specific PCR: a novel PCR assay for methylation status of CpG islands. *Proc Natl Acad Sci USA* **93** (18), 9821–9826.
- [25] Li LC and Dahiya R (2002). MethPrimer: designing primers for methylation PCRs. *Bioinformatics* **18** (11), 1427–1431.
- [26] Gregoire L, Rabah R, Schmelz EM, Munkarah A, Roberts PC, and Lancaster WD (2001). Spontaneous malignant transformation of human ovarian surface epithelial cells *in vitro*. *Clin Cancer Res* **7** (12), 4280–4287.
- [27] Sood AK, Fletcher MS, Coffin JE, Yang M, Seftor EA, Gruman LM, Gershenson DM, and Hendrix MJ (2004). Functional role of matrix metalloproteinases in ovarian tumor cell plasticity. *Am J Obstet Gynecol* **190** (4), 899–909.
- [28] Jones PA and Baylin SB (2002). The fundamental role of epigenetic events in cancer. *Nat Rev Genet* **3** (6), 415–428.
- [29] Maines-Bandiera SL, Kruk PA, and Auersperg N (1992). Simian virus 40-transformed human ovarian surface epithelial cells escape normal growth controls but retain morphogenetic responses to extracellular matrix. *Am J Obstet Gynecol* **167** (3), 729–735.
- [30] Nitta M, Katabuchi H, Ohtake H, Tashiro H, Yamaizumi M, and Okamura H (2001). Characterization and tumorigenicity of human ovarian surface epithelial cells immortalized by SV40 large T antigen. *Gynecol Oncol* **81** (1), 10–17.
- [31] Liu J, Yang G, Thompson-Lanza JA, Glassman A, Hayes K, Patterson A, Marquez RT, Auersperg N, Yu Y, Hahn WC, et al. (2004). A genetically defined model for human ovarian cancer. *Cancer Res* **64** (5), 1655–1663.
- [32] Flesken-Nikitin A, Choi KC, Eng JP, Shmidt EN, and Nikitin AY (2003). Induction of carcinogenesis by concurrent inactivation of p53 and Rb1 in the mouse ovarian surface epithelium. *Cancer Res* **63** (13), 3459–3463.
- [33] Connolly DC, Bao R, Nikitin AY, Stephens KC, Poole TW, Hua X, Harris SS, Vanderhyden BC, and Hamilton TC (2003). Female mice chimeric for expression of the simian virus 40 TAg under control of the MISIR promoter develop epithelial ovarian cancer. *Cancer Res* **63** (6), 1389–1397.
- [34] Godwin AK, Testa JR, Handel LM, Liu Z, Vanderveer LA, Tracey PA, and Hamilton TC (1992). Spontaneous transformation of rat ovarian surface epithelial cells: association with cytogenetic changes and implications of repeated ovulation in the etiology of ovarian cancer. *J Natl Cancer Inst* **84** (8), 592–601.
- [35] Testa JR, Getts LA, Salazar H, Liu Z, Handel LM, Godwin AK, and Hamilton TC (1994). Spontaneous transformation of rat ovarian surface epithelial cells results in well to poorly differentiated tumors with a parallel range of cytogenetic complexity. *Cancer Res* **54** (10), 2778–2784.
- [36] Stewart SL, Querec TD, Ochman AR, Gruver BN, Bao R, Babb JS, Wong TS, Koutroukides T, Pinnola AD, Klein-Szanto A, et al. (2004). Characterization of a carcinogenesis rat model of ovarian preneoplasia and neoplasia. *Cancer Res* **64** (22), 8177–8183.
- [37] Malaguamera L, Ferlito L, Di Mauro S, Imbesi RM, Scalia G, and Malaguamera M (2001). Immunosenescence and cancer: a review. *Arch Gerontol Geriatr* **32** (2), 77–93.
- [38] Kusyk CJ, Seski JC, Medlin WV, and Edwards CL (1981). Progressive chromosome changes associated with different sites of one ovarian carcinoma. *J Natl Cancer Inst* **66** (6), 1021–1025.
- [39] Maines-Bandiera SL and Auersperg N (1997). Increased E-cadherin expression in ovarian surface epithelium: an early step in metaplasia and dysplasia? *Int J Gynecol Pathol* **16** (3), 250–255.
- [40] MacCalman CD, Farookhi R, and Blaschuk OW (1994). Estradiol regulates E-cadherin mRNA levels in the surface epithelium of the mouse ovary. *Clin Exp Metastasis* **12** (4), 276–282.
- [41] Imai T, Horiuchi A, Wang C, Oka K, Ohira S, Nikaido T, and Konishi I (2003). Hypoxia attenuates the expression of E-cadherin via up-regulation of SNAIL in ovarian carcinoma cells. *Am J Pathol* **163** (4), 1437–1447.
- [42] Auersperg N, Pan J, Grove BD, Peterson T, Fisher J, Maines-Bandiera S, Somasiri A, and Roskelley CD (1999). E-cadherin induces mesenchymal-to-epithelial transition in human ovarian surface epithelium. *Proc Natl Acad Sci USA* **96** (11), 6249–6254.
- [43] Hirohashi S and Kanai Y (2003). Cell adhesion system and human cancer morphogenesis. *Cancer Sci* **94** (7), 575–581.
- [44] Wei SH, Chen CM, Stratthdee G, Hamsomburana J, Shyu CR, Rahmatpanah F, Shi H, Ng SW, Yan PS, Nephew KP, et al. (2002). Methylation microarray analysis of late-stage ovarian carcinomas distinguishes progression-free survival in patients and identifies candidate epigenetic markers. *Clin Cancer Res* **8** (7), 2246–2252.
- [45] Ahluwalia A, Yan P, Hurteau JA, Bigsby RM, Jung SH, Huang TH, and Nephew KP (2001). DNA methylation and ovarian cancer: I. Analysis of CpG island hypermethylation in human ovarian cancer using differential methylation hybridization. *Gynecol Oncol* **82** (2), 261–268.
- [46] Ahluwalia A, Hurteau JA, Bigsby RM, and Nephew KP (2001). DNA methylation in ovarian cancer: II. Expression of DNA methyltransferases in ovarian cancer cell lines and normal ovarian epithelial cells. *Gynecol Oncol* **82** (2), 299–304.
- [47] Zhu Y, Maric J, Nilsson M, Brannstrom M, Janson PO, and Sundfeldt K (2004). Formation and barrier function of tight junctions in human ovarian surface epithelium. *Biol Reprod* **71** (1), 53–59.
- [48] Yamasaki H, Omori Y, Zaidan-Dagli ML, Mironov N, Mesnil M, and Krutovskikh V (1999). Genetic and epigenetic changes of intercellular communication genes during multistage carcinogenesis. *Cancer Detect Prev* **23** (4), 273–279.
- [49] Umhauer S, Ruch RJ, and Fanning J (2000). Gap junctional intercellular communication and connexin 43 expression in ovarian carcinoma. *Am J Obstet Gynecol* **182** (5), 999–1000.
- [50] Mehta PP, Perez-Stable C, Nadji M, Mian M, Asotra K, and Roos BA (1999). Suppression of human prostate cancer cell growth by forced expression of connexin genes. *Dev Genet* **24** (1–2), 91–110.
- [51] Fernstrom MJ, Koffler LD, Abou-Rjaily G, Boucher PD, Shewach DS, and Ruch RJ (2002). Neoplastic reversal of human ovarian carcinoma cells transfected with connexin43. *Exp Mol Pathol* **73** (1), 54–60.
- [52] Esinduy CB, Chang CC, Trosko JE, and Ruch RJ (1995). *In vitro* growth inhibition of neoplastically transformed cells by non-transformed cells: requirement for gap junctional intercellular communication. *Carcinogenesis* **16** (4), 915–921.
- [53] Hernandez-Blazquez FJ, Joazeiro PP, Omori Y, and Yamasaki H (2001). Control of intracellular movement of connexins by E-cadherin in murine skin papilloma cells. *Exp Cell Res* **270** (2), 235–247.